LETTER

Condensation on slippery asymmetric bumps

Kyoo-Chul Park[1,2], Philseok Kim[2], Alison Grinthal[1], Neil He[1], David Fox[1], James C. Weaver[2] & Joanna Aizenberg[1,2,3]

Controlling dropwise condensation is fundamental to water-harvesting systems[1–3], desalination[4], thermal power generation[4–8], air conditioning[9], distillation towers[10], and numerous other applications[4,5,11]. For any of these, it is essential to design surfaces that enable droplets to grow rapidly and to be shed as quickly as possible[4–7]. However, approaches[4–8,10–21] based on microscale, nanoscale or molecular-scale textures suffer from intrinsic trade-offs that make it difficult to optimize both growth and transport at once. Here we present a conceptually different design approach—based on principles derived from Namib desert beetles[3,22–24], cacti[25], and pitcher plants[17,26]—that synergistically combines these aspects of condensation and substantially outperforms other synthetic surfaces. Inspired by an unconventional interpretation of the role of the beetle's bumpy surface geometry in promoting condensation, and using theoretical modelling, we show how to maximize vapour diffusion flux[20,27,28] at the apex of convex millimetric bumps by optimizing the radius of curvature and cross-sectional shape. Integrating this apex geometry with a widening slope, analogous to cactus spines, directly couples facilitated droplet growth with fast directional transport, by creating a free-energy profile that drives the droplet down the slope before its growth rate can decrease. This coupling is further enhanced by a slippery, pitcher-plant-inspired nanocoating that facilitates feedback between coalescence-driven growth and capillary-driven motion on the way down. Bumps that are rationally designed to integrate these mechanisms are able to grow and transport large droplets even against gravity and overcome the effect of an unfavourable temperature gradient. We further observe an unprecedented sixfold-higher exponent of growth rate, faster onset, higher steady-state turnover rate, and a greater volume of water collected compared to other surfaces. We envision that this fundamental understanding and rational design strategy can be applied to a wide range of water-harvesting and phase-change heat-transfer applications.

The central concepts for integrating the growth and transport of water droplets are derived from a combination of strategies used by three distinct biological examples—Namib desert beetles[3,22–24], cacti[25], and *Nepenthes* pitcher plants[26]—as summarized in Fig. 1. Several desert beetle species harvest water using their bumpy backs, but the topography of these surfaces has been overlooked, primarily because most previous studies attributed preferential condensation to surface chemistry (hydrophilic bumps with hydrophobic surroundings) and discounted convex topography as inferior to concave, on the basis of research into microscale and nanoscale textures[13,14,22,29,30]. However, the beetle bumps are large (millimetres across), and recent studies have reported that the entire bumpy surfaces are homogeneously covered with hydrophobic wax[23,24], thus questioning the role of localized surface chemistry in promoting condensation. We considered instead that even in the absence of localized chemical patterning or microscale/nanoscale textures, the specific geometry of convex millimetre-sized surface structures alone could facilitate condensation, and therefore the topography of synthetic bumpy surfaces could potentially be designed to optimize fast, localized droplet growth by focusing vapour diffusion flux[20,27,28] at the apex. We further hypothesized that fast growth of millimetre-sized droplets could be coupled to rapid directional turnover by integrating optimized apex geometry with an asymmetric slope analogous to that used by cactus spines to guide capillary-driven transport of harvested water drops. Lastly, the negligible friction of the slippery coating of pitcher plants inspired us to coat the bumps with molecularly smooth lubricant immobilized on nanotexture to facilitate these topography-based mechanisms.

To test the idea that droplets grow faster on convex millimetre-sized surface structures by focused diffusion flux, we measured the diameter of the largest droplet growing on the apex of a simple spherical-cap-shaped bump shown in Fig. 2a (see Supplementary Methods for the fabrication process, Supplementary Tables 1 and 2 for surface characterization, and Supplementary Fig. 1 for experimental setup). In this test, the depletion layer thickness δ (of the order of 10 mm), where convection normal to the surface is negligible, is much greater than the height of the cap ($H \approx 0.8 \pm 0.25$ mm), making diffusion of water vapour the dominant mass transport mechanism[28]. As shown in Fig. 2b, the diameter of
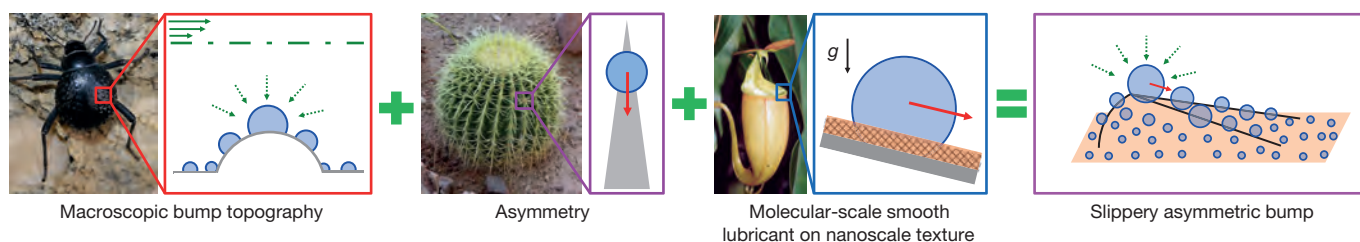

Figure 1 | An overview of our approach. The convex millimetric bump topography of water-harvesting desert beetles inspired the rational design of bumps that optimize fast, localized droplet growth by focusing vapour diffusion flux (green dotted arrows) at the apex. We further designed the bump to include an asymmetric slope analogous to that of cactus spines for capillary-guided directional transport of harvested droplets, and a pitcher-plant-inspired molecularly smooth lubricant immobilized on nanotexture. The green dash-dotted line represents the depletion layer. The green, black and red solid arrows represent the directions of convection, gravity *g* and drop transport, respectively. Approximate species dimensions are: desert beetle, 1.5 cm long; cactus, 20 cm in diameter; pitcher plant, 15 cm tall. Images are adapted with permission from Wikimedia Commons (desert beetle photograph by Hans Hillewaert, cactus photograph by Stan Shebs), and ref. 26 (pitcher plant photograph, copyright (2004) National Academy of Sciences, USA).

[1]John A. Paulson School of Engineering and Applied Sciences, Harvard University, Cambridge, Massachusetts, USA. [2]Wyss Institute for Biologically Inspired Engineering, Harvard University, Cambridge, Massachusetts, USA. [3]Department of Chemistry and Chemical Biology, Harvard University, Cambridge, Massachusetts, USA.
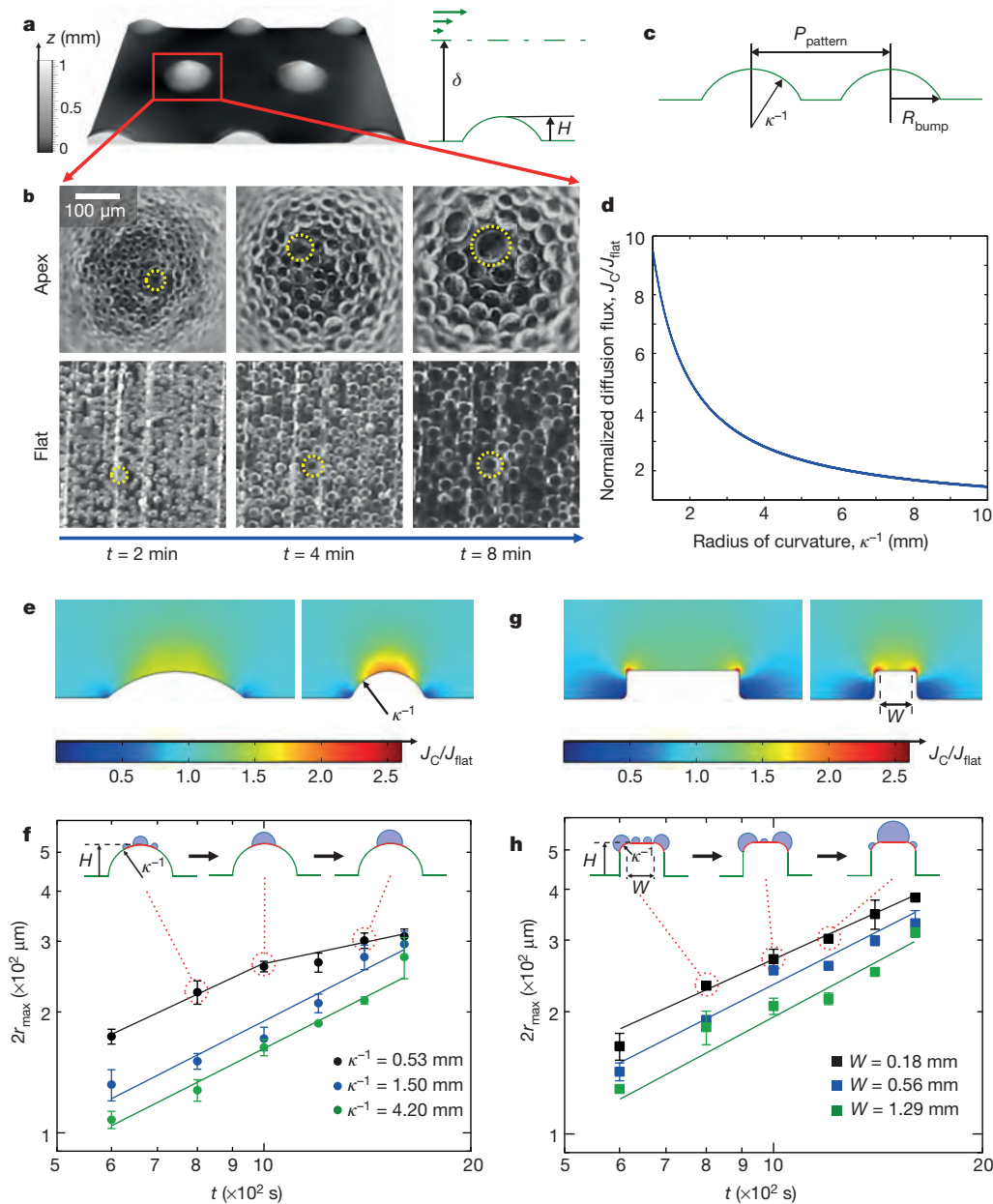
Figure 2 | Design of, and droplet growth on, convex bumps.
a, A profilometer image of a hexagonal array of millimetre-sized spherical-cap-shaped bumps (left), and the location of the plane (green dash-dotted line, right), below which diffusion is the dominant mechanism of mass transport (depletion layer thickness $\delta \gg H$). **b**, Time-lapsed images of droplets growing on the apex of the bumps (top row) compared to a flat region with the same height H (bottom row). Yellow circles indicate the largest droplet in each image (see Supplementary Video 1). **c**, A schematic illustration indicating the radius of curvature κ^{-1}, periodicity $P_{pattern}$, and half-bump width R_{bump}. **d**, Predicted diffusion flux J_C on the apex

of a spherical bump as a function of the radius of curvature κ^{-1} (see Supplementary Fig. 5 for the analytical model used in the derivation of J_C). (J_{flat} is the predicted diffusion flux on a flat surface with the same depletion layer thickness.) **e**, Numerically calculated intensity profile of diffusion flux (COMSOL-Multiphysics). **f**, Time-dependent droplet growth on bumps with decreasing radii of curvature. $2r_{max}$ is the averaged diameter of the three largest droplets. **g**, Numerical calculation of diffusion flux and quantitative analysis of droplet growth on rectangular bumps of width W. **h**, Time-dependent droplet growth on bumps with decreasing width. All error bars are 1 s.d.

the largest droplet on the apex of the bump, denoted by yellow dotted circles in the top images, is greater than that of a droplet on the nearby flat regions of the same surface (yellow dotted circles in the bottom images) at each time point (see Supplementary Video 1). Detailed studies were performed to rule out the role of surface roughness, chemistry and temperature differences in promoting such site-specific droplet growth (see the 'Control Experiments' section of the Supplementary Information, Supplementary Video 2, and Supplementary Figs 2–4 for discussion). These initial results indicate that the convex macroscopic surface topography—positive radius of curvature κ^{-1} in Fig. 2c—plays an important part in controlling diffusion flux.

To optimize the focused diffusion flux, we developed predictive models that quantify the magnitude and spatial profile of vapour flux as a function of the radius of curvature. A plot of the simple scaling of diffusion flux near the apex of a spherical cap ($J_C \propto 1/\kappa^{-1}$; see the 'Theoretical modelling' section of the Supplementary Information and Supplementary Fig. 5 for a detailed derivation) shows that the smaller the radius of curvature, the greater the localized diffusion flux (Fig. 2d). Numerical calculation (Fig. 2e) using the COMSOL-Multiphysics program (https://www.comsol.com/comsol-multiphysics) enables us to visualize more precisely the spatial distribution and intensity of diffusion flux on the bump and surrounding flat regions.
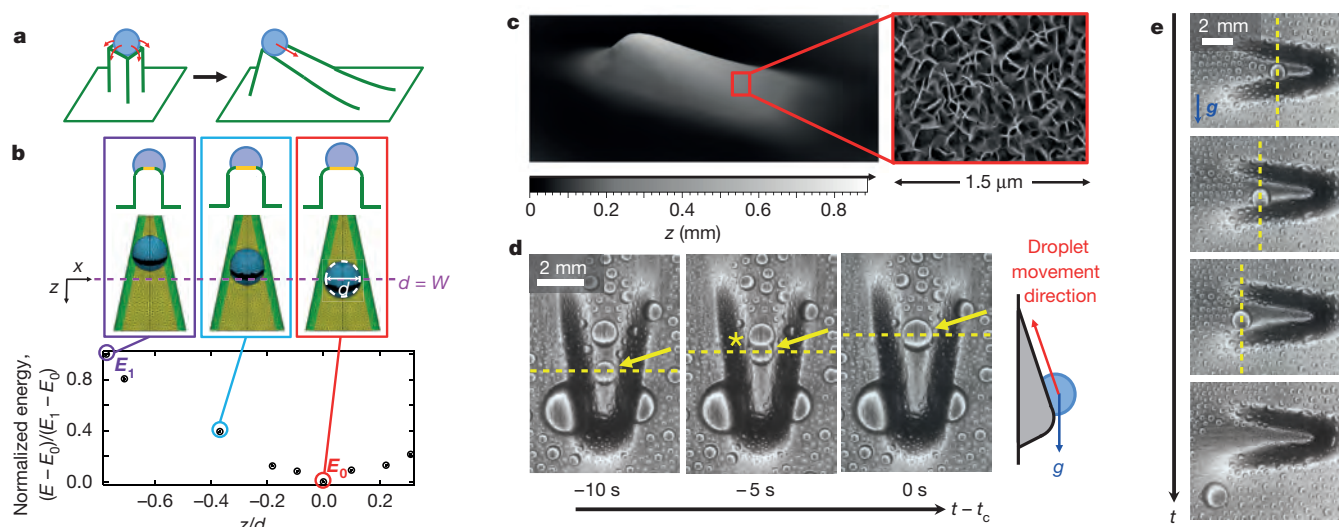
Figure 3 | Capillary-driven transport. a, Transport (red arrows) on a rectangular bump (left) and an asymmetric slope (right). **b,** Energy profile of the asymmetric bump–droplet–vapour system, obtained by finite-element-based numerical calculation (Surface Evolver). E_1 and E_0 represent the calculated energy values of the system in the purple and red boxes, respectively. **c,** A profilometer image (oblique view) showing nanostructure (inset) infused with lubricant, and the tangentially connected bottom slope. **d, e,** Time-lapsed optical images of condensed water droplets on an asymmetric bump rotated 180° (**d**) and 90° (**e**) relative to gravity, corresponding to Supplementary Video 3 (starting at

running time ~19 s) and Supplementary Video 4 (starting at running time ~8 s). The droplet shown by the yellow arrow partially covers the curved border (indicated by a higher reflection that can be seen as a thin bright region between the black sides and the grey flat top) of the asymmetric bump ($t - t_c = -10$ s, where t_c is the time of completed coalescence). The yellow asterisk indicates coalescence with another drop. The dotted yellow line tracks the vertical (**d**) or horizontal (**e**) progress of the droplet. See Supplementary Videos 3–5 for more information about the role of a gradually widening slope.

As indicated by the red to yellow colour gradient, the area where the diffusion flux is greater than on the flat region with the same height becomes increasingly concentrated at and around the apex, and its maximum intensity grows stronger, as the radius of curvature decreases.

Consistent with the analytical and numerical models, we experimentally observe the largest droplet diameters at the apex of spherical-cap-shaped surface features that have the smallest radii of curvature (Fig. 2f, Supplementary Table 3). However, the rate of droplet growth on the bump with the smallest radius of curvature begins to slow down at later time points (see black curve in Fig. 2f). This change of slope suggests that the effect of the focused diffusion flux at the apex diminishes when this region (represented by the red colour in the illustration in Fig. 2f) becomes covered by the growing droplet. To maintain the advantages of the small radius of curvature but avoid this decrease in growth rate, we changed the geometry of the apex from spherical to rectangular, with a flat region on top bordered by rounded edges as shown in Fig. 2g and h. This shape allows us to incorporate an even smaller radius of curvature around the perimeter, combined with an additional area of focused flux on the top flat area. For a smaller width, the superposition of diffusion flux focused on these features collectively results in a larger contiguous area of high diffusion flux. Droplets on the rectangular structure, therefore, continue growing for a longer time at a constant growth rate, as shown in Fig. 2h, because the coalescence and movement of the growing droplets to the flat top area of the bump continues to provide fresh sites for re-nucleation and growth.

As the growing droplet begins to cover the curved edges, the shape of the rectangular structure—flat with curved borders—also lends itself to a mechanism to transport the droplet directionally, when topographical asymmetry is integrated into the design. Whereas a droplet growing on a rectangular column will eventually fall off in a random direction (Fig. 3a), the addition of a gradually widening slope descending from one side is expected to promote downward motion by enabling the drop to transition to a completely flat surface. As shown by the numerical calculation (Supplementary Fig. 6) the total free energy of the droplet–bump–vapour system is lowest when the droplet is on a completely flat region of such an asymmetric convex structure where the diameter of a droplet d equals the width of the underlying asymmetric convex

structure W (Fig. 3b). Simulation (using the Surface Evolver program; http://facstaff.susqu.edu/brakke/evolver/evolver.html) suggests that the capillary force resulting from this energy profile on a surface with negligible friction would lead the drop to move down the slope towards the wider flat area (represented by the yellow surface in Fig. 3b) such that it will no longer overlap with the curved regions.

To experimentally validate the latter hypothesis, we fabricated asymmetric bumps with a tangential connection between the descending slope and the surrounding flat regions (Fig. 3c). The negligible friction and pinning assumed in the numerical calculation were achieved by incorporating the pitcher-plant-inspired slippery nanocoating[11,17,18] on top of the entire surface. On the fabricated slippery asymmetric structures, droplets move even against gravity (Fig. 3d and Supplementary Video 3) because in such a system the capillary effect is dominant compared to gravitational effect (as captured by the Bond number—the ratio between gravitational force and capillary force—which is ($\rho_{water} - \rho_{air})gr^2/\gamma_{LV} \approx 1/7$ at the length scale of the droplet, where ρ_{water} and ρ_{air} are the density of water and air, g is the gravitational constant, r is the radius of the droplet, and γ_{LV} is the surface tension of the water–vapour interface). In addition, even though the lowest energy point for the moving droplet with a constant diameter is not the bottom of the bump (that is, its widest region) and the droplet might be expected to be pinned upon reaching the point where $d = W$, the droplet (indicated by a yellow arrow in Fig. 3d) keeps moving and accelerating as its size grows by coalescing with other small droplets on its path (for example, as indicated by an asterisk in Fig. 3d), thus continuing to satisfy the condition $d > W$. This mechanism guides droplet motion solely along the direction determined by the widening slope, regardless of the orientation of the bump relative to gravity, as shown in Fig. 3e and Supplementary Videos 4 and 5.

When surface structures are designed to optimize and integrate all of these mechanisms cooperatively, droplets rapidly grow and start to shed much earlier than on other state-of-the-art surfaces. Figure 4a provides quantitative analysis of the droplet growth as a function of time, comparing the performance of slippery and superhydrophobic surfaces with and without asymmetric bumps. In agreement with earlier studies[6,7,11,17], flat slippery surfaces outperform superhydrophobic
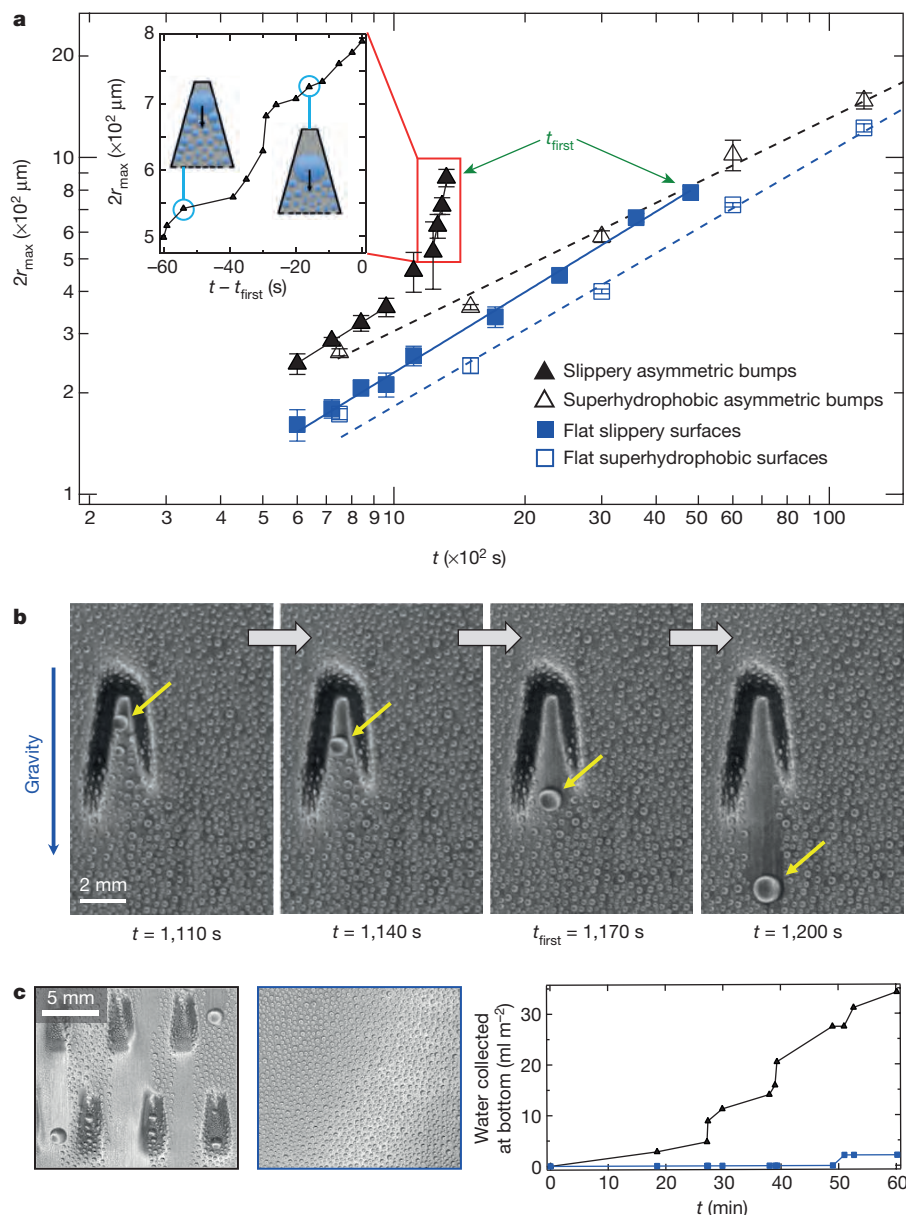
Figure 4 | Coupled fast growth and transport. a, Quantitative analysis of growth dynamics and shedding compared to state-of-the-art surfaces. Both slippery asymmetric bumps and superhydrophobic asymmetric bumps show faster localized droplet growth in the early stage ($t < 10^3$ s) compared to flat slippery and superhydrophobic control surfaces. Each data point represents the averaged value of the largest droplet's growth on each of three different bumps, or locations in the case of flat surfaces. The red box indicates further enhanced growth rate on slippery asymmetric bumps. t_{first} is the average time at which the first three drops

are transported solely by gravity. Each data point in the red box represents the average size of these three drops. The inset shows a magnified view of the fast growth. All error bars are 1 s.d. **b**, Time-lapsed images of droplets condensed on slippery surfaces. **c**, An exemplary array of the slippery asymmetric bumps (left image, black line in the plot) shows a substantially greater volume of water collected at the bottom of the surface (see Supplementary Video 6), compared to the flat slippery surfaces (right image, blue line in the plot).

surfaces in droplet size measured at a given time. Moreover, owing to the higher diffusion flux at the apex of the convex features, both slippery asymmetric bumps (solid black line) and superhydrophobic asymmetric bumps (dotted black line) show faster localized droplet growth in the early stage ($t < 10^3$ s) than do their flat controls. Even more interestingly, surfaces with slippery asymmetric bumps show a unique discontinuous behaviour, with a slope of ~0.82 at the early stage and ~6.4 at the later stage of droplet growth, which is more than six-fold higher than the maximum slope (~1) observed in typical droplet growth dynamics[27,28]. Supplementary Figs 7 and 8 demonstrate the importance of combining all the described features of the multi-scale surface structures in achieving successful droplet growth and transport: the absence of any of the design components noticeably slows down

droplet growth dynamics. The accelerated growth (slope of 6.4) captured by the magnified view in the inset of Fig. 4a (see Supplementary Fig. 9 for more information about the accelerated growth of individual droplets compared to other controls) can be interpreted as the feedback between coalescence-driven growth and capillary-driven transport discussed above. As a result, the fast-growing droplets on the slippery asymmetric bumps, which are aligned with gravitational force, are delivered to the bottom of the slope at a size where they can then be transported by gravity, while droplets on the adjacent flat slippery surfaces are still far below the critical shedding diameter (Fig. 4b).

In our experiments, droplets shed from the slippery bumps within $t_{first} \approx 10^3$ s (where t_{first} is the average time at which the first three drops are transported solely by gravity), whereas droplets on

other state-of-the-art surfaces grow slowly, and shed much later (for example, $t_{first} \approx 4 \times 10^3$ s on flat slippery surfaces) or do not shed for more than $t \approx 10^4$ s (for example, on superhydrophobic surfaces and all other controls shown in Supplementary Figs 7 and 8). Owing to this faster droplet growth and transport performance, which yields a continuous, rapid steady-state turnover, a slippery surface with an exemplary array of the asymmetric structures designed in this study (Fig. 4c and Supplementary Video 6) shows a volume of water turnover an order of magnitude greater than that of the flat slippery surfaces and other state-of-the-art surfaces (for which $t_{first} > 200$ min as shown in Fig. 4a and Supplementary Fig. 7) developed for dropwise condensation[4–7,11,12,15,17–20].

Further analysis of the steady-state turnover kinetics over 7 h (Supplementary Fig. 10) highlights that the volume of water collected on the slippery surfaces with asymmetric structures progressively outpaces that collected on the control surface, with the advantage continuously becoming greater with time even after both reach t_{first}. By coupling fast growth and fast transport, the integrated bump design not only eliminates the long onset delay observed on other surfaces but also yields a substantially higher steady-state turnover rate. This combination of short response time and reliable, high-volume long-term performance are critical in numerous applications based on condensation, transport, and phase-change heat transfer, such as heat exchange, dehumidification, and desalination systems. The central principles derived in this work further enable the manipulation of drop behaviour against an unfavourable temperature gradient. Although larger droplets are expected at a colder surface, a drop at the apex of a bump with a small radius of curvature shows the opposite trend: increased drop size at higher temperature (Supplementary Fig. 4a). This unusual behaviour is relevant to pipe geometry, an analogous form of convex curvature that is widely used in phase-change heat transfer (Supplementary Fig. 4b).

In summary, we have achieved unprecedented droplet growth and transport by designing surfaces covered with slippery asymmetric bumps based on quantitative models that integrate three mechanisms—(1) optimization of focused diffusion flux by the radius of curvature and shape of the apex, (2) asymmetric topography that guides the droplet off the bump by optimizing the free-energy profile, and (3) positive feedback between capillary transport and continued growth by coalescence along the slope.

The rapid turnover kinetics, with fast onset and sustained continuous shedding rate, combined with the ability to defy a temperature gradient, are crucial not only for water-harvesting applications, particularly in hot, arid regions where condensed water droplets will evaporate if they do not shed after a limited time, but also for many phase-change heat-transfer applications requiring reliable steady-state performance. It may also be possible to create switchable water-transporting surfaces with flexible topographical features that can be tuned by external stimuli, and to discover fundamental principles of droplet growth and transport in practical and more complex situations such as with strong airflow.

1. Clus, O., Ortega, P., Muselli, M., Milimouk, I. & Beysens, D. Study of dew water collection in humid tropical islands. *J. Hydrol.* **361,** 159–171 (2008).
2. Zheng, Y. *et al.* Directional water collection on wetted spider silk. *Nature* **463,** 640–643 (2010).
3. Malik, F. T., Clement, R. M., Gethin, D. T., Krawszik, W. & Parker, A. R. Nature's moisture harvesters: a comparative review. *Bioinspir. Biomim.* **9,** 031002 (2014).
4. Miljkovic, N. *et al.* Jumping-droplet-enhanced condensation on scalable superhydrophobic nanostructured surfaces. *Nano Lett.* **13,** 179–187 (2013).
5. Rose, J. W. Dropwise condensation theory and experiment: a review. *Proc. Inst. Mech. Eng. A* **216,** 115–128 (2002).
6. Xiao, R., Miljkovic, N., Enright, R. & Wang, E. N. Immersion condensation on oil-infused heterogeneous surfaces for enhanced heat transfer. *Sci. Rep.* **3,** 1988 (2013).
7. Anand, S., Paxson, A. T., Dhiman, R., Smith, J. D. & Varanasi, K. K. Enhanced condensation on lubricant-impregnated nanotextured surfaces. *ACS Nano* **6,** 10122–10129 (2012).
8. Daniel, S., Chaudhurry, M. K. & Chen, J. C. Fast drop movements resulting from the phase change on a gradient surface. *Science* **291,** 633–636 (2001).
9. Pérez-Lombard, L., Ortiz, J. & Pout, C. A review on buildings energy consumption information. *Energy Build.* **40,** 394–398 (2008).
10. Rykaczewski, K. *et al.* Dropwise condensation of low surface tension fluids on omniphobic surfaces. *Sci. Rep.* **4,** 4158 (2014).
11. Kim, P. *et al.* Liquid-infused nanostructured surfaces with extreme anti-ice and anti-frost performance. *ACS Nano* **6,** 6569–6577 (2012).
12. Quéré, D. Wetting and roughness. *Annu. Rev. Mater. Res.* **38,** 71–99 (2008).
13. Mishchenko, L., Khan, M., Aizenberg, J. & Hatton, B. D. Spatial control of condensation and freezing on superhydrophobic surfaces with hydrophilic patches. *Adv. Funct. Mater.* **23,** 4577–4584 (2013).
14. Varanasi, K. K., Hsu, M., Bhate, N., Yang, W. & Deng, T. Spatial control in the heterogeneous nucleation of water. *Appl. Phys. Lett.* **95,** 094101 (2009).
15. Nosonovsky, M. & Bhushan, B. Superhydrophobic surfaces and emerging applications: non-adhesion, energy, green engineering. *Curr. Opin. Colloid Interf. Sci.* **14,** 270–280 (2009).
16. Courbin, L. *et al.* Imbibition by polygonal spreading on microdecorated surfaces. *Nature Mater.* **6,** 661–664 (2007).
17. Wong, T.-S. *et al.* Bioinspired self-repairing slippery surfaces with pressure-stable omniphobicity. *Nature* **477,** 443–447 (2011).
18. Carlson, A., Kim, P., Amberg, G. & Stone, H. A. Short and long time drop dynamics on lubricated substrates. *Europhys. Lett.* **104,** 34008 (2013).
19. Krupenkin, T. N., Taylor, J. A., Schneider, T. M. & Yang, S. From rolling ball to complete wetting: the dynamic tuning of liquids on nanostructured surfaces. *Langmuir* **20,** 3824–3827 (2004).
20. Medici, M.-G., Mongruel, A., Royon, L. & Beysens, D. Edge effects on water droplet condensation. *Phys. Rev. E* **90,** 062403 (2014).
21. Fratzl, P. & Weinkamer, R. Nature's hierarchical materials. *Prog. Mater. Sci.* **52,** 1263–1334 (2007).
22. Parker, A. R. & Lawrence, C. R. Water capture by a desert beetle. *Nature* **414,** 33–34 (2001).
23. Nørgaard, T. & Dacke, M. Fog-basking behaviour and water collection efficiency in Namib Desert Darkling beetles. *Front. Zool.* **7,** 23 (2010).
24. Guadarrama-Cetina, J. *et al.* Dew condensation on desert beetle skin. *Eur. Phys. J. E* **37,** 109 (2014).
25. Ju, J. *et al.* A multi-structural and multi-functional integrated fog collection system in cactus. *Nature Commun.* **3,** 1247 (2012).
26. Bohn, H. F. & Federle, W. Insect aquaplaning: *Nepenthes* pitcher plants capture prey with the peristome, a fully wettable water-lubricated anisotropic surface. *Proc. Natl Acad. Sci. USA* **101,** 14138–14143 (2004).
27. Viovy, J. L., Beysens, D. & Knobler, C. M. Scaling description for the growth of condensation patterns on surfaces. *Phys. Rev. A* **37,** 4965–4970 (1988).
28. Beysens, D. Dew nucleation and growth. *C. R. Phys.* **7,** 1082–1100 (2006).
29. Zhai, L. *et al.* Patterned superhydrophobic surfaces: toward a synthetic mimic of the Namib Desert beetle. *Nano Lett.* **6,** 1213–1217 (2006).
30. Qian, M. & Ma, J. Heterogeneous nucleation on convex spherical substrate surfaces: a rigorous thermodynamic formulation of Fletcher's classical model and the new perspectives derived. *J. Chem. Phys.* **130,** 214709 (2009).

Author Contributions K.-C.P., P.K. and J.A. conceived the research. J.A. supervised the research. K.-C.P., P.K. and J.A. designed the slippery asymmetric bumps and the experiments. K.-C.P., P.K., N.H., D.F. and J.C.W. carried out the experiments. All authors analysed data. K.-C.P. built the analytical and numerical models. K.-C.P., P.K., A.G., D.F. and J.A. interpreted data and wrote the paper.

Author Information Reprints and permissions information is available at www.nature.com/reprints. The authors declare competing financial interests: details are available in the online version of the paper. Readers are welcome to comment on the online version of the paper. Correspondence and requests for materials should be addressed to K.-C.P. (kpark@seas.harvard.edu) or J.A. (jaiz@seas.harvard.edu).